Analytical thermal model for end-pumped solid-state lasers

L Cini[1,2]**, J I Mackenzie**[2]

[1] Dipartimento di Fisica, Università di Pisa, Largo B. Pontecorvo 3, Pisa, 56127, Italy, Fax: 050 2214634, Email: luigi.cini@outlook.com

[2] Optoelectronics Research Centre, University of Southampton, Highfield, Southampton, SO17 1BJ, United Kingdom, Fax: (0)23 8059 3142, Email: jim@orc.soton.ac.uk

Abstract Fundamentally power-limited by thermal effects, the design challenge for end-pumped "bulk" solid-state lasers depends upon knowledge of the temperature gradients within the gain medium. We have developed analytical expressions that can be used to model the temperature distribution and thermal-lens power in end-pumped solid-state lasers. Enabled by the inclusion of a temperature-dependent thermal conductivity, applicable from cryogenic to elevated temperatures, typical pumping distributions are explored and the results compared with accepted models. Key insights are gained through these analytical expressions, such as the dependence of the peak temperature rise in function of the boundary thermal conductance to the heat sink. Our generalized expressions provide simple and time-efficient tools for parametric optimization of the heat distribution in the gain medium based upon the material and pumping constraints.

1 Introduction

The end-pumped solid-state laser is a mature design architecture exploited for many scientific, industrial and medical laser applications, in the tens-of-watts power regime. Cost effective, compact, and relatively efficient, in recent decades their performance has capitalized on improving diode laser brightness and power. Further power-scaling however, is fundamentally limited by the thermo-optical properties of the gain medium and the induced optical distortions, primarily driven by the quantum defect between pump and the emission wavelengths. Alternatively, the geometry of the gain medium can be optimized to enhance thermal management and minimize the thermal lensing effects, such as the thin-disk [1], fibre [2], or slab architectures [3], which have demonstrated

multi-kW average powers. Nonetheless, for many applications the end-pumped bulk architecture still holds an important position for its simplicity and robust performance.

The basic design strategy for these lasers has been to try to mitigate the effects of the induced thermal lensing and aberrations [4]. As such it is important to understand the induced temperature distribution over the active volume of interest, that is, where the cavity mode passes through the excited region of the gain medium. Typically this involves numerical simulations solving the heat equation with finite element algorithms, having almost completely replaced analytical solutions due to the complexity of the necessary assumptions made in order to obtain exact expressions. Analytical solutions though, are unquestionably important: they highlight qualitative and quantitative features of underlying physical phenomena and provide more accurate solutions in far less time than numerical calculations, particularly if trying to perform parameter-dependence studies. One strict assumption generally made in determining the exact solution for the temperature profile along an end-pumped solid-state laser is that the thermal conductivity of the crystal is not significantly dependent on temperature [5]. While a reasonable assumption for many active media, operating at and above room temperature (RT), it is generally not valid when cooled to a cryogenic temperature (CT) [6]. Here the gradient for the changing thermal conductivity with respect to temperature steepens

considerably compared with the same around RT. With this argument in mind, and therefore including a temperature dependence for the thermal conductivity in the heat conduction equation, it is possible to exploit integral transforms to reach analytical solutions [7].

In this paper, we use the Kirchhoff transform [8] to convert the non-linear heat equation into a solvable linear equation for a cylindrical radially isotropic gain element. Analytical solutions for the temperature distribution along the length of a side-cooled end-pumped rod are presented for different pump distributions that can be used for practical configurations, such as near-diffraction-limited, to fibre-coupled diode-laser, pumps. Furthermore, this result provides novel analytical expressions for the thermal-lens strength associated with the pump-induced accumulated optical phase shift, which converge to well-known equations [5] when a temperature-independent thermal conductivity is chosen.

The rest of this paper is organized as follows: we start by introducing the model for the thermal conductivity $k(T)$, which matches with actual measurements and provides simple solutions for the Kirchhoff transform, and its dependence over the two main temperature ranges of practical interest. Utilizing this form for $k(T)$ the derivation of the exact solutions for the temperature distribution along an end-pumped rod are given. Four different pump distributions are studied to cover commonly used pump sources, and to make direct comparison with previous work; these include the top-hat, Gaussian, gener-

alized n-th order super-Gaussian, and annular (donut) distributions. At this point the importance of the heat transfer coefficient, h, at the boundary between rod and heat sink, is highlighted. An expression is derived that relates the pumping parameters to a minimum critical value for h, below which, the temperature at the centre of rod rises rapidly. In the penultimate section the expressions for the thermal lens strength, now calculable at any temperature in the CT and well above RT regimes, are derived, and then compared with the two extremes reported in the literature, i.e. top-hat and Gaussian. The solution for the Gaussian pump is derived as a special solution to the generalized SG distribution. Finally, to end the paper we summarize with conclusions and appendices for detailed workings.
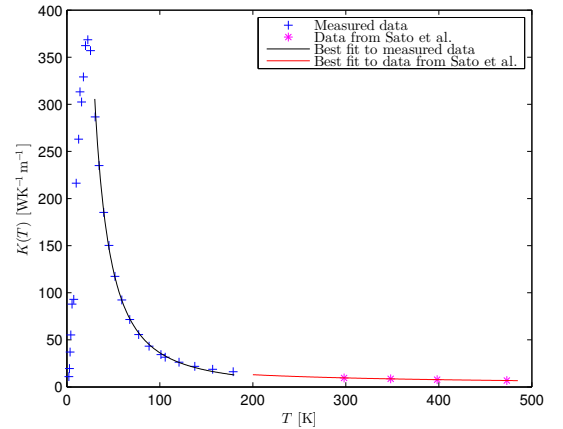
2   Temperature dependence of thermal conductivity

We focus our attention on the Nd:YAG crystal. Since YAG is a cubic crystal, the thermal conductivity can be considered as a scalar quantity. The dependence on temperature of the thermal conductivity can be modeled by the following formula:

$$k(T) = k_0 \left(\frac{T}{T_0} \right)^m \qquad (1)$$

where k_0, T_0 and m results from a best fit to measured data. Since these parameters strictly depend on the doping level of the rare-earth ion, we choose a particular doping concentration, say $\sim 1\%$. We performed two best

fits for two different temperature ranges around CT and RT. The first fit is based on measured data on a 1.3 at.% Nd:YAG sample in a temperature range of 40 K$\leq$ $T \leq$175 K [10], while the second is based on published data of Sato et al. [11] relating to 1.2 at.% Nd:YAG in a temperature range of 300 K$\leq$ T $\leq$475 K. By finding the intersection of the two fitting curves, a common value of T_0 and $k_0 = k(T_0)$ for the two temperature ranges can be found. The values of the parameters for $\sim$1 at.% Nd:YAG are therefore: $T_0 = 164.17$ K, $k_0 = 15.09$ WK^{-1}m^{-1}, $m_{\mathrm{CT}} = -1.77$, and $m_{\mathrm{RT}} = -0.75$. The data used and the corresponding best fits curves are shown in Figure 1.

Fig. 1 Measured thermal conductivity dependance on temperature, after [10,11], and best fits using Equation (1).

2.1   Temperature dependence of thermal conductivity for selected materials

In Table 1 the values of k_0, T_0 and m are provided for Nd:YAG at different temperatures, along with different

doping concentrations and a variety of other interesting host materials, including some that would not normally be considered for an end-pumped rod architecture, rather more appropriate to a thin disk geometry. These values result from a best fit of Equation (1) to available data from published literature [6, 11, 12]. As previously mentioned, the thermal conductivity can be considered a scalar quantity strictly for isotropic laser crystals. However, since in this thermal model a pure radial heat flux will be assumed (see Section 3), uniaxial laser materials can also be included and, in this case, only the dependance on temperature along the a-axes is considered.

3   Analytical solution

The steady state heat conductance equation, with temperature-dependent thermal conductivity and different end-pumping profiles, governing the system shown in Figure 2, is:

$$\nabla \cdot [k(T)\nabla T(r, z)] + S(r, z) = 0 \qquad (2)$$

where $k(T)$ is the temperature-dependent thermal conductivity and $S(r, z)$ is the thermal power per unit volume dissipated in the laser rod.

The edge of the rod is considered to be surrounded by a heat sink, held at a constant temperature, T_c, by active cooling. Heat transfer across the boundary between the laser rod and the heat sink is described by the heat transfer coefficient or surface conductance, h. The end faces are instead supposed to be in contact with air, with

Table 1 Thermal conductivity parameters for selected materials.

Crystal	T [K]	k_0 $\left[\frac{W}{Km}\right]$	T_0 [K]	m
YAG[a]	80-300	17.29	199.96	-1.57
1.3 at.% Nd:YAG	40-175	15.09	164.17	-1.77
2 at.% Yb:YAG[a]	80-300	12.59	199.45	-1.46
4 at.% Yb:YAG[a]		11.72	199.38	-1.17
15 at.% Yb:YAG[a]		9.08	199.25	-0.87
LuAG[a]		12.06	199.43	-1.14
YLF(a)[a]		8.31	199.17	-1.57
5 at.% Yb:YLF(a)[a]		5.74	199.24	-1.04
LuLF(a)[a]		7.86	199.13	-1.65
GGG [b]	100-300	12.19	199.44	-1.25
CY$_2$O$_3$[b]		20.43	200.37	-1.19
GdVO$_4$(a)[b]		13.71	199.57	-1.30
YAG[c]	300-475	14.00	199.58	-0.78
0.7 at.% Nd:YAG[c]		13.55	199.56	-0.77
0.9 at.% Nd:YAG[c]		13.36	199.56	-0.77
1.2 at.% Nd:YAG[c]		15.09	164.17	-0.75
5.0 at.% Yb:YAG[c]		8.98	199.22	-0.56
9.4 at.% Yb:YAG[c]		8.12	199.19	-0.54
22.9 at.% Yb:YAG[c]		6.86	199.16	-0.48

References: a- [6], b- [12] and c- [11].

negligible heat flux through them. An equivalent h_{ef} coefficient can be calculated for the end faces [15] and since typically $h >> h_{ef}$ the assumption of pure radial heat flux can be made [5]. Furthermore, it is assumed in the following that the diameter of the pumped region is significantly smaller than the inverse of the absorption co-
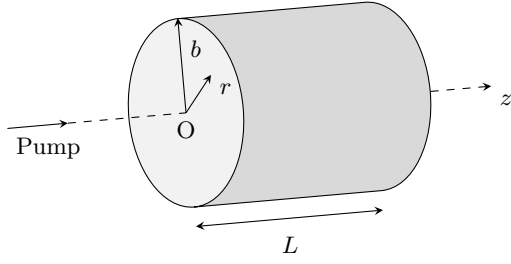
Fig. 2 End-pumped laser rod representation. Point O is located at $r = 0$ and $z = 0$.

efficient, reinforcing the statement of radial heat flux. It follows that the longitudinal derivatives in Equation (2) with respect to the corresponding radial derivatives [14], can be neglected. Here it's also assumed that the pump profile is axisymmetric, the behavior of the thermal conductivity $k(T)$ of the crystal is described by Equation (1) and the cooling is isotropic in the z-plane. These assumptions allow us to write Equation (2) as

$$\frac{1}{r}\frac{d}{dr}\left[rk(T)\frac{dT(r,z)}{dr}\right] + S(r,z) = 0 \qquad (3)$$

Equation (3) can be solved introducing an integral transform (Kirchhoff transform) in terms of a function U defined as [8]:

$$U(r,z) = \int^{T} k(\tau)d\tau \qquad (4)$$

By the fundamental theorem of calculus,

$$k(T) = \frac{dU}{dT} \qquad (5)$$

and, substituting Equation (5) into Equation (3) and using the chain rule of differentiation, Equation (3) is transformed into the linear equation:

$$\nabla^2 U(r,z) = \frac{1}{r}\frac{dU(r,z)}{dr} + \frac{d^2U(r,z)}{dr^2} = -S(r,z) \qquad (6)$$

that can be easily solved for different pump distributions and the actual temperature can be determined by the inverse Kirchhoff transform.

Using Equation (1), one obtains

$$U = \frac{k_0}{(m+1)T_0^m}T^{m+1} + C \qquad (7)$$

where C is an arbitrary constant of integration. It is important to note that Equation (7) is not valid if $m = -1$; however, the temperature distribution in this case has already been derived by Hodgson and Weber for a side-pumped laser rod [9].

The four different pump distributions studied in this paper, corresponding to four different $S(r,z)$ terms in Equation (6), are shown in Figure 3 at $z = 0$ (see Section 3.1 for the value of the parameters considered). They are respectively the top-hat (TH), Gaussian (G), super-Gaussian (SG) and donut (D). Two super-Gaussian profiles are reported in the figure, one for the 4th order and the other for 8th order.
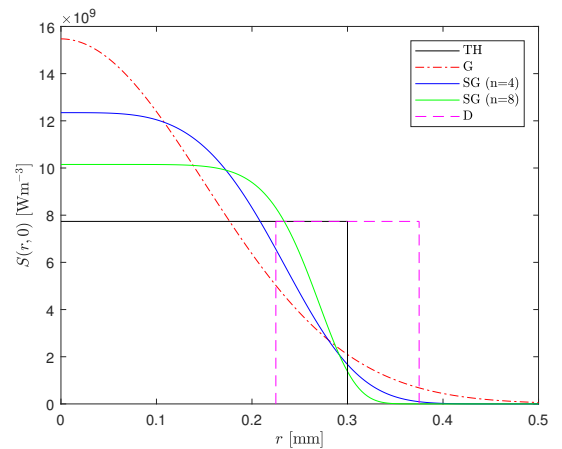
Fig. 3 Different heat source distributions considered. The total heating power for each is 5.16 W.

3.1 Top-hat Pumping

Although not a typically realistic pump distribution for end-pumped lasers, the top-hat profile is the simplest starting solution, which can be easily compared with previous literature studies ([15], [5]). Consider the following thermal loading distribution:

$$S(r, z) = \begin{cases} Q_0 e^{-\alpha z} & 0 \leq r \leq a \\ 0 & a < r \leq b \end{cases} \tag{8}$$

where Q_0 is a normalization constant, α is the pump absorption coefficient, a is the radius of the pumping beam and b is the radius of the laser rod. The normalization constant Q_0 can be calculated using the following relation

$$Q_0 = \frac{\eta_h P}{V} \tag{9}$$

where $\eta_h P$ is the total heating power (η_h is the fractional thermal load) and V is the volume of the pump-photon distribution in the rod, where it is assumed that there are insignificant energy migration effects and the heat source is created at the point of pump-photon absorption, i.e.

$$V = \int_0^{2\pi} d\varphi \int_0^a r dr \int_0^L e^{-\alpha z} dz = \frac{\pi a^2 \eta_{abs}}{\alpha} \tag{10}$$

where $1 - e^{-\alpha L} = \eta_{abs}$ is the absorption efficiency. Substituting Equations (9) and (10) into Equation (8), the thermal power per unit volume dissipated into the laser rod becomes:

$$S(r, z) = \begin{cases} \dfrac{\eta_h P_{\text{in}} \alpha e^{-\alpha z}}{\pi a^2} & 0 \leq r \leq a \\ 0 & a < r \leq b \end{cases} \tag{11}$$

where P_{in} is the incident pump power.

Equation (6) is solved separately between $0 \leq r \leq a$ and $a < r \leq b$, resulting in two functions U_1 and U_2 respectively, leading to two temperature solutions, $T_1(r, z)$ and $T_2(r, z)$ in the respective regions, as shown in Appendix A. These solutions are:

$$T_1(r, z) = \left\{ F_0 e^{-\alpha z} \left[1 - \frac{r^2}{a^2} + \ln\left(\frac{b^2}{a^2}\right) \right] \right. \\ \left. + \left(T_c + \frac{\eta_h P_{\text{in}} \alpha e^{-\alpha z}}{2\pi b h} \right)^{m+1} \right\}^{\frac{1}{m+1}} \tag{12}$$

for $0 \leq r \leq a$ and

$$T_2(r, z) = \left[F_0 e^{-\alpha z} \ln\left(\frac{b^2}{r^2}\right) \right. \\ \left. + \left(T_c + \frac{\eta_h P_{\text{in}} \alpha e^{-\alpha z}}{2\pi b h} \right)^{m+1} \right]^{\frac{1}{m+1}} \tag{13}$$

for $a < r \leq b$, where F_0 is a constant defined as:

$$F_0 = \frac{\eta_h P_{\text{in}} \alpha (m+1) T_0^m}{4\pi k_0} \tag{14}$$

Figure 4 shows the calculated temperature distribution using Equations (12) and (13) with the following parameters: $b = 1.25$ mm, $L = 5$ mm, $a = 300$ μm, $P_{\text{in}} = 25$ W, $\eta_h = 0.25$, $T_c = 300$ K, $\alpha = 350$ m^{-1} and $h = 2$ WK^{-1}cm^{-2} (the choice of this value for h will be discussed in Section 4).

The temperature-independent thermal conductivity case can be obtained from Equations (12) and (13) setting $m = 0$. In this way the temperature distribution inside the rod is given by

$$\Delta T(r, z) = \frac{\eta_h P_{\text{in}} \alpha e^{-\alpha z}}{4\pi k_0} \begin{cases} 1 - \dfrac{r^2}{a^2} + \ln\left(\dfrac{b^2}{a^2}\right) & 0 \leq r \leq a \\ \ln\left(\dfrac{b^2}{r^2}\right) & a < r \leq b \end{cases} \tag{15}$$
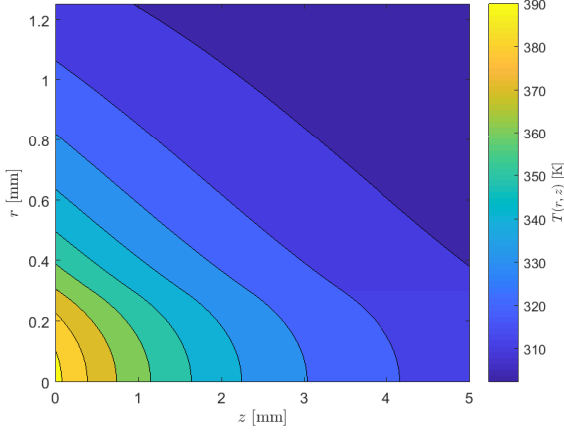
**Fig. 4** Temperature profile of a top-hat end-pumped laser rod.

where $\Delta T(r, z) = T(r, z) - T(b, z)$. Equation (15) shows the well-know quadratic radial dependance of the temperature inside the pumped region of the rod and the logarithmic dependance outside [15]. In Figure 5 a comparison, at the pumped surface of the rod, $z = 0$, for $\Delta T(r, z)$ considering a temperature-dependent thermal conductivity, and Equation (15), is shown. The parameters for this comparison are the same as those for Figure 4. The constant thermal conductivity in Equation (15) is evaluated using Equation (1) at $T = T_c$.

3.1.1 Temperature Profile for different coolant temperatures Maintaining the same thermal load conditions, whilst lowering the temperature of the heat sink surrounding the Nd:YAG crystal, which is an artificial example as the spectroscopic proprieties of the gain medium also change [13], a decrease in the maximum temperature rise at the center of the crystal is obtained. This is due to the corresponding increase in the thermal conduc-
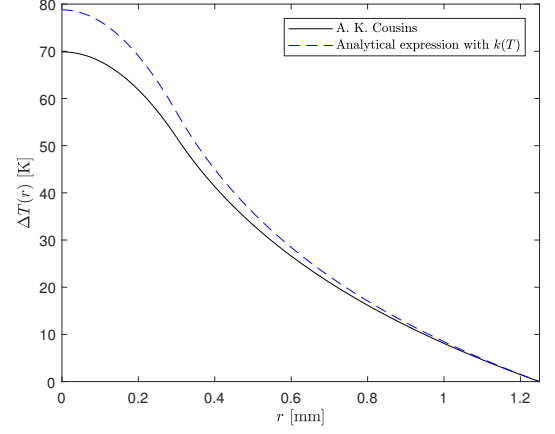
Fig. 5 Comparison between our analytical temperature difference profile in the case of RT top-hat pumping and the one published by Cousins [15].

tivity as shown in Figure 1. Equations (12) and (13) can be used to have a quantitative measure of this effect. In Figure 6 the temperature rise is calculated with the same parameters above and different coolant temperatures.
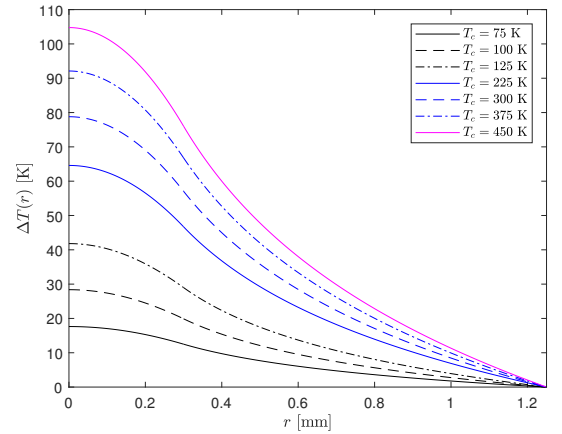
Fig. 6 Temperature difference profile for the same thermal load conditions as Figure 5 but with different coolant temperatures. At $T_c = 225$ K the thermal conductivity is extrapolated from the RT expression.

3.2 Gaussian Pumping

A more realistic and often used pumping distribution employing a diffraction-limited pump, is a Gaussian, defined as

$$S(r,z) = Q_0 e^{-2\frac{r^2}{w^2}} e^{-\alpha z} \quad (16)$$

where w is the $1/e^2$ radius of the intensity profile of the pump beam. The volume of the heated region is given by

$$V = \frac{\pi}{2} w^2 \left(1 - e^{-2\frac{b^2}{w^2}}\right) \frac{\eta_{abs}}{\alpha} \quad (17)$$

and the term in the brackets in the Equation (17) can be set to unity in most cases of interest, where the pump beam is significantly smaller than the radius of the laser rod. Using Equations (9) and (16), the heat source becomes:

$$S(r,z) = \frac{2\eta_h P_{\text{in}}\alpha}{\pi w^2} e^{-2\frac{r^2}{w^2}} e^{-\alpha z} \quad (18)$$

Thus Equation (6) in the case of Gaussian pumping is

$$\frac{1}{r}\frac{dU}{dr} + \frac{d^2U}{dr^2} = -\frac{2\eta_h P_{\text{in}}\alpha}{\pi w^2} e^{-2\frac{r^2}{w^2}} e^{-\alpha z} \quad (19)$$

and with the following boundary conditions

$$\left.\frac{dU}{dr}\right|_{r=0} = 0 \quad (20a)$$

$$\left.\frac{dU}{dr}\right|_{r=b} = h\left[T_c - T(r=b)\right] \quad (20b)$$

yields:

$$T(r,z) = \left\{ F_0 e^{-\alpha z} \left[\ln\left(\frac{b^2}{r^2}\right) + E_1\left(\frac{2b^2}{w^2}\right)\right.\right.$$
$$\left.\left. - E_1\left(\frac{2r^2}{w^2}\right)\right] + \left[T_c + \frac{\eta_h P_{\text{in}}\alpha e^{-\alpha z}}{2\pi bh}\right]^{m+1} \right\}^{\frac{1}{m+1}} \quad (21)$$

where $E_1(u)$ is the exponential integral defined as

$$E_1(u) = \int_1^\infty \frac{e^{-ut}}{t} dt. \quad (22)$$

Note that if a temperature-independent thermal conductivity (i.e. $m = 0$) is considered, Equation (21) becomes

$$T(r,z) = \frac{\eta_h P_{\text{in}}\alpha e^{-\alpha z}}{4\pi k_0} \left[\ln\left(\frac{b^2}{r^2}\right) + E_1\left(\frac{2b^2}{w^2}\right)\right.$$
$$\left. - E_1\left(\frac{2r^2}{w^2}\right)\right] + T_c + \frac{\eta_h P_{\text{in}}\alpha e^{-\alpha z}}{2\pi bh} \quad (23)$$

which gives a temperature difference between the center and the edge of the rod equal to

$$\Delta T(r,z) = \frac{\eta_h P_{\text{in}}\alpha e^{-\alpha z}}{4\pi k_0} \left[\ln\left(\frac{b^2}{r^2}\right) + E_1\left(\frac{2b^2}{w^2}\right)\right.$$
$$\left. - E_1\left(\frac{2r^2}{w^2}\right)\right] \quad (24)$$

For $P_h = \eta_h P_{\text{in}}$, Equation (24) is the same result as the one published by Innocenzi et al. [14]. Figure 7 shows a comparison between our temperature profile and the one published by Innocenzi et al. with the same parameters used for the top-hat case ($w = 300$ μm is chosen). Also in this case, the constant thermal conductivity is evaluated using Equation (1) at $T = T_c$.
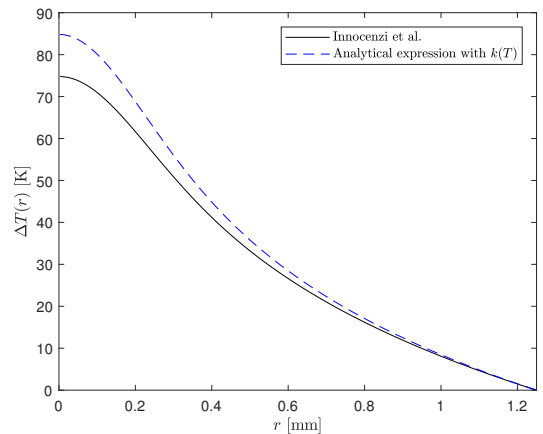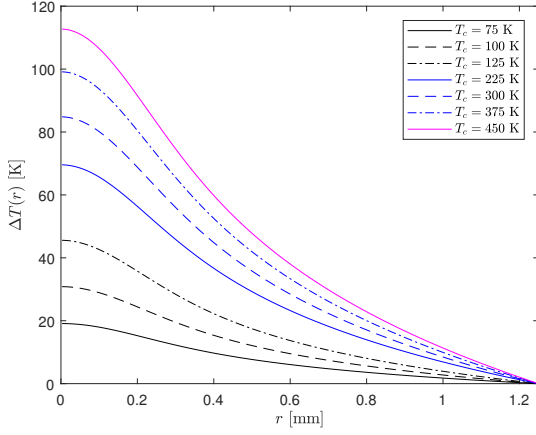

Fig. 7 Comparison between our analytical temperature difference profile in the case of Gaussian pumping and the one published by Innocenzi [14].

In Figure 8 the analytical temperature difference pro-

files with the same parameters above, but for different coolant temperatures, are again shown.

Fig. 8 Temperature difference profile for the same thermal load conditions as Figure 7 but with different coolant temperatures.

3.3 Generalized n-th order Super-Gaussian

Often in the case of higher-power solid-state lasers, fiber-coupled diode-laser pumps are employed. For a substantial part of the pump distribution in the laser rod, the pump can be approximated by a super-Gaussian. The heat source considered is

$$S(r,z) = Q_0 e^{-\alpha z} e^{-2\frac{r^n}{w^n}} \tag{25}$$

where n is an even integer. The volume of the heated region can be found as

$$
\begin{aligned}
V = {} & \int_0^{2\pi} d\varphi \int_0^b r e^{-2\frac{r^n}{w^n}} dr \int_0^L e^{-\alpha z} dz = \\
& 2\pi \frac{4^{-\frac{1}{n}} w^2}{n} \left[\Gamma\left(\frac{2}{n},0\right) - \Gamma\left(\frac{2}{n}, 2\frac{b^n}{w^n}\right) \right] \frac{\eta_{\text{abs}}}{\alpha}
\end{aligned}
\tag{26}
$$

where $\Gamma(a,x)$ is the incomplete gamma function. For $n=2$, $b=1.25$ mm and $w=300$ μm, $\Gamma\left(\frac{2}{n}, 2\frac{b^n}{w^n}\right) \approx$

10^{-15} and since for higher values of n this term is even smaller, it can be safely ignored. Furthermore, by definition, $\Gamma\left(\frac{2}{n},0\right) = \Gamma\left(\frac{2}{n}\right)$, so the normalized heat source is

$$S(r,z) = \frac{n\eta_h P_{\text{in}}\alpha}{2\pi 4^{-\frac{1}{n}} w^2 \Gamma\left(\frac{2}{n}\right)} e^{-\alpha z} e^{-2\frac{r^n}{w^n}} \tag{27}$$

Figure 9 shows the heat sources for n=2, 4, 8, 16 and 32 at $z=0$ with the following parameter values: $w=300$ μm, P_{in}=25 W, $\eta_h = 0.25$, $\alpha = 350$ m^{-1}.
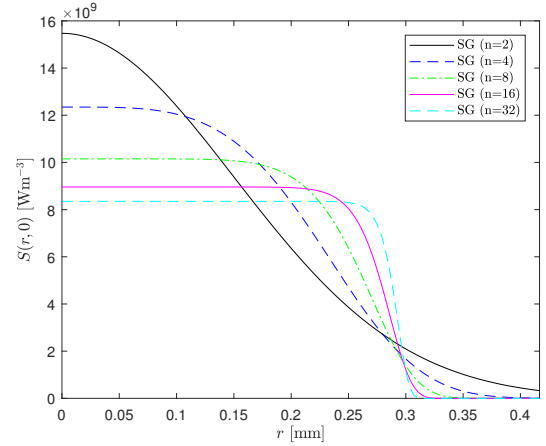
Fig. 9 Heat source distributions in the case of super-Gaussian pumping.

Substituting Equation (27) into Equation (6), and using the same boundary conditions of the previous section, the temperature profile inside the end-pumped laser rod is found to be:

$$
\begin{aligned}
T(r,z) = {} & \\
& \left\{ G_0 e^{-\alpha z} \left[b^2 {}_2F_2\left(\frac{2}{n}, \frac{2}{n}; 1+\frac{2}{n}, 1+\frac{2}{n}; -\frac{2b^n}{w^n}\right) \right. \right. \\
& \left. - r^2 {}_2F_2\left(\frac{2}{n}, \frac{2}{n}; 1+\frac{2}{n}, 1+\frac{2}{n}; -\frac{2r^n}{w^n}\right) \right] \\
& \left. + \left(T_c + \frac{\eta_h P_{\text{in}}\alpha e^{-\alpha z}}{2\pi b h}\right)^{m+1} \right\}^{\frac{1}{m+1}}
\end{aligned}
\tag{28}
$$

where

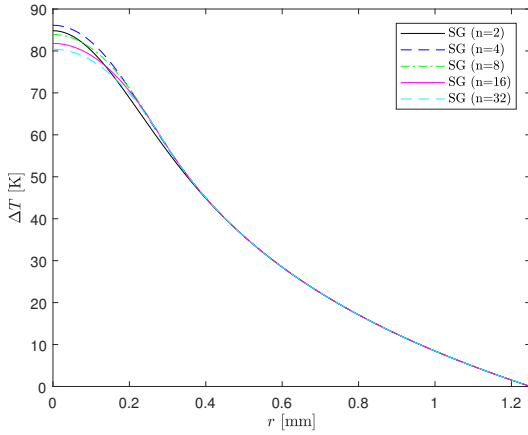$$G_0 = \frac{2^{\left(\frac{2}{n}-1\right)} n F_0}{\Gamma\left(\frac{2}{n}\right) w^2}, \quad (29)$$

$_pF_q\left(a_1, ..., a_p; b_1, ..., b_q; z\right)$ is the Generalized Hypergeometric Function, defined as

$$_pF_q\left(a_1, ..., a_p; b_1, ..., b_q; z\right) = \sum_{k=0}^{\infty} \frac{(a_1)_k...(a_p)_k}{(b_1)_k...(b_q)_k} \frac{z^k}{k!} \quad (30)$$

and $(x)_k$ stands for the Pochhammer symbol, i.e.,

$$(x)_k = \frac{\Gamma(x+k)}{\Gamma(x)} = x(x+1)...(x+k-1) \quad (31)$$

Figures 10 and 11 show Equation (28) for $n=2, 4, 8, 16$ and 32 at $z = 0$ with the same values of the parameters used in the previous sections at RT.

Fig. 10 Temperature difference profile in the case of super-Gaussian pumping.

The center temperature is found to be maximum in the case of $n = 4$. This is quite surprising, since one might have expected that it increases going from the TH ($n = \infty$) to G pump profile ($n = 2$). A more in-depth analysis, varying both the transversal dimension of the crystal and the pump laser waist in Equation (28), shows that
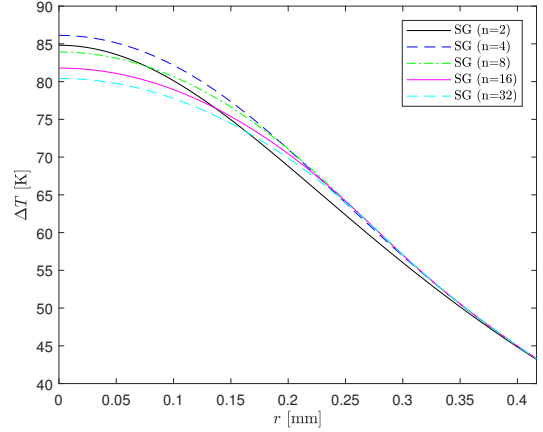
Fig. 11 Temperature difference profile in the case of super-Gaussian pumping (zoom).

the relationship between the center temperatures in Figures 10 and 11 remains the same. Indeed, this does not depend on the lab parameters, but rather on how G_0 and

$$_2F_2\left(\frac{2}{n}, \frac{2}{n}; 1+\frac{2}{n}, 1+\frac{2}{n}; -\frac{2b^n}{w^n}\right)$$

depend on n.

However, $T(0,0)$ is not included in the calculation of the thermal dioptric power of the pumped rod, which does follow the expected trend (see Section 5). It will be shown that what matters is the coefficient of the quadratic term in the Taylor expansion of the temperature distribution, whose modulus is maximum in the case of G pumping and decreases in the SG pumping case as n increases.

3.3.1 Gaussian solution as the special case of the super-Gaussian with $n = 2$ It can be shown for the special case of $n = 2$ in Equation (28) that its solution for the temperature profile is the same as that derived from the

Gaussian distribution (Equation (21)). In this case, the Generalized Hypergeometric Function in Equation (28) corresponds to

$$
_2F_2\left(1,1;2,2;z\right)=\sum_{k=0}^{\infty}\frac{(1)_k(1)_k}{(2)_k(2)_k}\frac{z^k}{k!} \tag{32}
$$

From Equation (31)

$$
(1)_k = k! \tag{33a}
$$

$$
(2)_k = (k+1)! \tag{33b}
$$

and substituting these values into Equation (32), one obtains

$$
\begin{aligned}
_2F_2\left(1,1;2,2;z\right)&=\sum_{k=0}^{\infty}\frac{1}{(k+1)^2}\frac{z^k}{k!}=\\
&\sum_{k=0}^{\infty}\frac{1}{k+1}\frac{z^{k+1}}{z(k+1)!}=\\
&\frac{1}{z}\sum_{k+1=1}^{\infty}\frac{1}{k+1}\frac{z^{k+1}}{(k+1)!}
\end{aligned} \tag{34}
$$

By the definition of the exponential integral:

$$
E_i(x)=\gamma+\ln|x|+\sum_{n=1}^{\infty}\frac{x^n}{nn!}, \tag{35}
$$

Equation (32) becomes:

$$
_2F_2\left(1,1;2,2;z\right)=\frac{1}{z}\left[-\gamma-\ln|z|+E_i(z)\right] \tag{36}
$$

Substituting Equation (36) into (28) with $n = 2$, the temperature profile is found to be exactly as Equation (21).

3.4 Donut Pumping

Finally, a fourth pump distribution that can be exploited to excite higher-order LG cavity modes is a donut shape

[16]. This can be described by:

$$
S(r,z)=\begin{cases}0 & 0\leq r\leq d_1\\[2mm]\dfrac{\eta_h P_{\mathrm{in}}\alpha}{\pi(d_2^2-d_1^2)}e^{-\alpha z} & d_1<r\leq d_2\\[2mm]0 & d_2<r\leq b\end{cases} \tag{37}
$$

Using the same procedure explained in the previous sections, the following temperature distributions can be obtained, respectively for $0\leq r\leq d_1$, $d_1<r\leq d_2$ and $d_2<r\leq b$:

$$
\begin{aligned}
T_1(z)=\Bigg\{&F_0e^{-\alpha z}\frac{d_2^2-d_1^2+d_2^2\ln\left(\frac{b^2}{d_2^2}\right)-d_1^2\ln\left(\frac{b^2}{d_1^2}\right)}{d_2^2-d_1^2}\\
&+\left[T_c+\frac{\eta_h P_{\mathrm{in}}\alpha e^{-\alpha z}}{2\pi bh}\right]^{m+1}\Bigg\}^{\frac{1}{m+1}}
\end{aligned} \tag{38}
$$

$$
\begin{aligned}
T_2(r,z)=\Bigg\{&F_0e^{-\alpha z}\frac{d_2^2-r^2+d_2^2\ln\left(\frac{b^2}{d_2^2}\right)-d_1^2\ln\left(\frac{b^2}{r^2}\right)}{d_2^2-d_1^2}\\
&+\left[T_c+\frac{\eta_h P_{\mathrm{in}}\alpha e^{-\alpha z}}{2\pi bh}\right]^{m+1}\Bigg\}^{\frac{1}{m+1}}
\end{aligned} \tag{39}
$$

and

$$
\begin{aligned}
T_3(r,z)=\Bigg\{&F_0e^{-\alpha z}\ln\left(\frac{b^2}{r^2}\right)\\
&+\left[T_c+\frac{\eta_h P_{\mathrm{in}}\alpha e^{-\alpha z}}{2\pi bh}\right]^{m+1}\Bigg\}^{\frac{1}{m+1}}
\end{aligned} \tag{40}
$$

Also in this case, the temperature distribution reduces to the known literature-reported result if $m = 0$ is imposed (see the very recent paper of Kim et al. [18]).

A summary of all the analytical temperature solutions obtained at $z = 0$ are shown in Figure 12. To ensure a valid comparison with the other temperature solutions, for the donut pump, $d_1 = 0.225$ mm and $d_2 = 0.375$ mm have been chosen. In this way the volume of the

pump-photon distribution in the rod is the same for all the pump distributions.
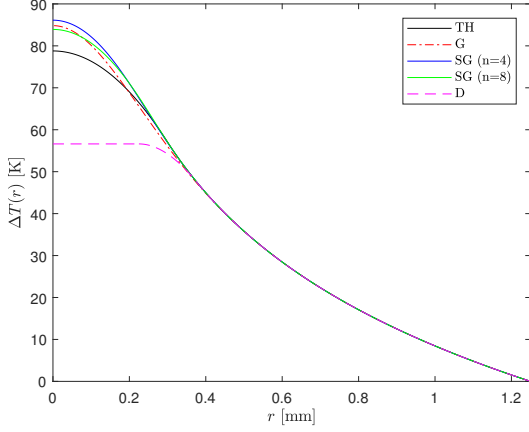
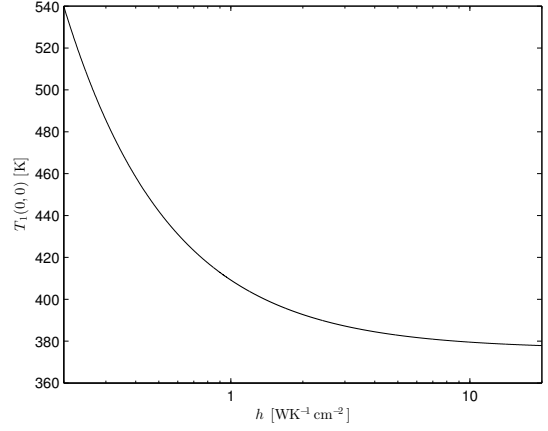**Fig. 12** Analytical solutions of the heat equation for each distribution considered.

3.1, with $T_c = 300$ K. As one can see from these figures

Fig. 13 Dependence of the maximum temperature on h

Fig. 14 Dependence of the derivative of the maximum temperature with respect to h on h

4 A brief digression on the heat transfer coefficient

The heat transfer coefficient, h, and its influence on the temperature distribution in this thermal model deserves a special mention. For the sake of simplicity, we limit our discussion to the pump-input surface, $z = 0$, where the maximum rise of temperature is expected. In the case of a top-hat pumping distribution, from Equation (12), the maximum temperature is given by
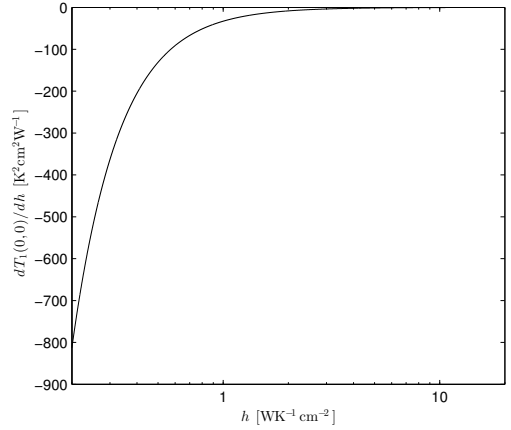
$$T_1(0,0) = \left\{ F_0 \left[1 + \ln \left(\frac{b^2}{a^2} \right) \right] + \left(T_c + \frac{\eta_h P_{\text{in}} \alpha}{2\pi bh} \right)^{m+1} \right\}^{\frac{1}{m+1}} \quad (41)$$

Figures 13 and 14 show respectively the dependance of Equation (41), and its derivative with respect to h, on h. Input parameters chosen are the same as in Section

and as one would expect, an increasing h implies that the maximum temperature rise asymptotes to a minimum constant value. Since this constant value is strictly reached at $h = \infty$ (i.e. in the case of perfect cooling), it is not easy to define an expression for a critical value of h, below which the maximum temperature rises rapidly. However, from the only h-dependent term in Equation

(41), one can define the limiting case, such that if

$$\frac{\eta_h P_{\text{in}} \alpha}{2\pi b T_c} << h \qquad (42)$$

then the dependance of $T_1(0,0)$ on h can be ignored. For the parameters used in this paper the left-hand side of Equation (42) is approximately equal to $0.093\,\text{WK}^{-1}\text{cm}^{-2}$. As it can be seen this value is just off the scale in Figures 13 and 14, and ultimately a tolerable increase in the peak temperature rise would have to be chosen to find a critical value for h. For example a 1% increase with respect to T_c (e.g. at 300 K) would imply a critical value for $h \sim 9.3\,\text{WK}^{-1}\text{cm}^{-2}$. This is five times higher than the best value reported by Chénais et al. [5], when employing heat sink grease as the thermal interface to a copper mount.

4.0.1 Dependance of the temperature rise on h To date the effect of h has only been related to the temperature difference across the boundary layer, since from the temperature-independent thermal conductivity model, the temperature difference between the center of the rod and the boundary does not depend on h [5]. As can be seen from Equations (41) and (13) this is no longer true when considering $k(T)$, as expressed in:

$$T_1(0,0) - T_2(b,0) =$$

$$\left\{ F_0 \left[1 + \ln\left(\frac{b^2}{a^2}\right) \right] + \left(T_c + \frac{\eta_h P_{\text{in}} \alpha}{2\pi b h} \right)^{m+1} \right\}^{\frac{1}{m+1}} \qquad (43)$$

$$- T_c - \frac{\eta_h P_{\text{in}} \alpha}{2\pi b h}$$

(note that setting $m = 0$ this dependence disappears).

Actually this is quite intuitive when considering $k(T)$,

as h, resulting mainly in a different temperature at the boundary of the rod, therefore changes the thermal conductivity of the rest of the laser crystal.

5 Analytical expression for the thermal lens power

Consider first the case of top-hat pumping and assume $h = \infty$, i.e. use the approximation of *perfect cooling*. A Taylor expansion can be performed at $r \approx 0$, giving

$$T(r,z) = \left\{ F_0 e^{-\alpha z} \left[1 + \ln\left(\frac{b^2}{a^2}\right) \right] + T_c^{m+1} \right\}^{\frac{1}{m+1}}$$

$$- \frac{F_0 e^{-\alpha z} \left\{ F_0 e^{-\alpha z} \left[1 + \ln\left(\frac{b^2}{a^2}\right) \right] + T_c^{m+1} \right\}^{-\frac{m}{m+1}}}{a^2(m+1)} r^2$$

$$+ O(r^3) \qquad (44)$$

and the approximation of $T^2(r,z)$ at $r \approx 0$ is instead

$$T^2(r,z) = \left\{ F_0 e^{-\alpha z} \left[1 + \ln\left(\frac{b^2}{a^2}\right) \right] + T_c^{m+1} \right\}^{\frac{2}{m+1}}$$

$$- \frac{2 F_0 e^{-\alpha z} \left\{ F_0 e^{-\alpha z} \left[1 + \ln\left(\frac{b^2}{a^2}\right) \right] + T_c^{m+1} \right\}^{\frac{1-m}{m+1}}}{a^2(m+1)} r^2$$

$$+ O(r^3) \qquad (45)$$

Figure 15 shows the agreement of the approximate function (44) in the pumped region ($r \leq a$) of the laser rod at $z = 0$ for the RT.

In a similar manner as detailed by Hodgson et al. [19], we consider the thermo-optic coefficient increasing linearly with temperature, i.e.

$$\chi(T) = \chi_0 + \chi_1 T \qquad (46)$$
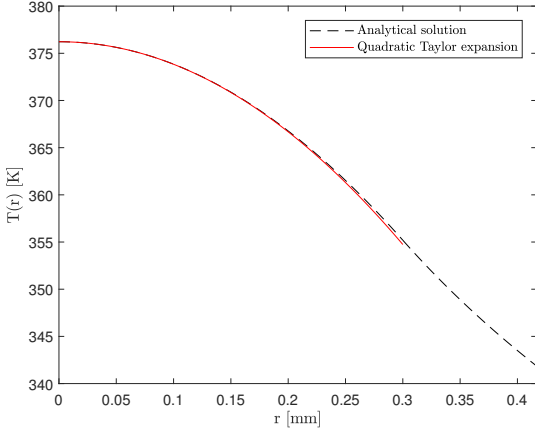
Fig. 15 Analytical solution and its Taylor expansion inside the pumped region in the approximation of *perfect cooling* at $z = 0$.

Then utilizing the definition for the optical path difference (OPD) [17]

$$\text{OPD}(r) = \int_0^L \chi(T)T(r,z)dz \tag{47}$$

and substituting Equation (46) into Equation (47), one obtains

$$\text{OPD}(r) = \chi_0 \int_0^L T(r,z)dz + \chi_1 \int_0^L T^2(r,z)dz \tag{48}$$

Furthermore using

$$\text{OPD}(0) - \text{OPD}(r) = \frac{D_{th}r^2}{2} \tag{49}$$

the thermal lens dioptric power is found to be

$$D_{th} = \frac{2\chi_0 F_0}{a^2(m+1)}$$
$$\cdot \int_0^L e^{-\alpha z} \left\{ F_0 e^{-\alpha z} \left[1 + \ln\left(\frac{b^2}{a^2}\right) \right] + T_c^{m+1} \right\}^{-\frac{m}{m+1}} dz$$
$$+ \frac{4\chi_1 F_0}{a^2(m+1)}$$
$$\cdot \int_0^L e^{-\alpha z} \left\{ F_0 e^{-\alpha z} \left[1 + \ln\left(\frac{b^2}{a^2}\right) \right] + T_c^{m+1} \right\}^{\frac{1-m}{m+1}} dz \tag{50}$$

which gives (see Appendix B for details)

$$D_{th} = \frac{2}{a^2\alpha \left[1 + \ln\left(\frac{b^2}{a^2}\right) \right]}$$
$$\cdot \left\{ \chi_0 \left[\left(F_0 e^{-\alpha z} \left[1 + \ln\left(\frac{b^2}{a^2}\right) \right] + T_c^{m+1} \right)^{\frac{1}{m+1}} \right]_L^0 \right.$$
$$\left. + \chi_1 \left[\left(F_0 e^{-\alpha z} \left[1 + \ln\left(\frac{b^2}{a^2}\right) \right] + T_c^{m+1} \right)^{\frac{2}{m+1}} \right]_L^0 \right\} \tag{51}$$

Note that, thanks to the particular dependence on r and z on the temperature distribution (Equation (44)), a higher-order polynomial fit equation for the thermo-optic coefficient could also be used, i.e.

$$\chi(T) = \sum_{i=0}^N \chi_i T^i, \tag{52}$$

in which case the thermal lens dioptric power is found to be

$$D_{th} = \frac{2}{a^2\alpha \left[1 + \ln\left(\frac{b^2}{a^2}\right) \right]} \sum_{i=0}^N \left\{ \chi_i \right.$$
$$\left. \cdot \left[\left(F_0 e^{-\alpha z} \left[1 + \ln\left(\frac{b^2}{a^2}\right) \right] + T_c^{m+1} \right)^{\frac{i+1}{m+1}} \right]_L^0 \right\} \tag{53}$$

Finally, in the case of temperature-independent thermal conductivity ($m = 0$), and, thermo-optic coefficient ($\chi_1 = 0$), it is remarkable that Equation (51) reduces to the well-known result for the thermal lens dioptric power generated in a TH end-pumped laser rod [5]:

$$D'_{th} = \frac{\chi_0 \eta_h P_{\text{in}} \eta_{abs}}{2\pi k_0 a^2} \tag{54}$$

A similar analysis can also be followed in the case of SG pumping (and then of G if $n = 2$ is considered), whereby

the thermal lens dioptric power is given by

$$D_{th} = \frac{2}{\alpha b^2 {}_2F_2} \left\{ \chi_0 \left[\left(G_0 b^2 {}_2F_2 e^{-\alpha z} + T_c^{m+1} \right)^{\frac{1}{m+1}} \right]_L^0 \right.$$
$$\left. + \chi_1 \left[\left(G_0 b^2 {}_2F_2 e^{-\alpha z} + T_c^{m+1} \right)^{\frac{2}{m+1}} \right]_L^0 \right\}$$

$$(55)$$

where, for the sake of simplicity, the constant

$${}_2F_2 \left(\frac{2}{n}, \frac{2}{n}; 1 + \frac{2}{n}, 1 + \frac{2}{n}; -\frac{2b^n}{w^n} \right)$$

is indicated just with ${}_2F_2$.

Again this result contracts to the well known one for the thermal lens dioptric power generated by a Gaussian-beam end-pumped laser rod in the case of constant thermal conductivity and thermo-optic coefficient ($n = 2$, $m = 0$ and $\chi_1 = 0$) [14]:

$$D'_{th} = \frac{\chi_0 \eta_h P_{\text{in}} \eta_{abs}}{\pi k_0 w^2}. \qquad (56)$$

Figure 16 shows the thermal lens powers as a function of the coolant temperature in both ranges (CT and RT), defined in Section 2, for four different pump distributions with the same parameters of Figure 4. Two different linear expressions for the thermo-optic coefficient are used, for the CT and RT ranges, corresponding to the valid temperature ranges for the thermal conductivity fits. The values utilized for χ_0 and χ_1 for each range have been found as follows.

Consider the thermo-optic coefficient defined as [17]

$$\chi(T) = \frac{dn}{dT}(T) + C_\alpha(n_0 - 1)(1 + \nu)\alpha_T(T) \qquad (57)$$

where $dn/dT(T)$ is the thermal dispersion, C_α is a parameter between 0 and 1 that includes the limitation of

a heated element of the rod in the free expansion along the longitudinal direction, due to the colder surrounding, if a transversely localized temperature increase occurs, ν is the Poisson's ratio, n_0 is the refractive index and $\alpha_T(T)$ the thermal expansion coefficient. Supposing both the thermal dispersion and the thermal expansion coefficient linearly depend upon temperature, i.e.

$$\frac{dn}{dT}(T) = l_0 + l_1 T \qquad (58)$$

and

$$\alpha_T(T) = l_2 + l_3 T, \qquad (59)$$

Equation (57) becomes

$$\chi(T) = l_0 + C_\alpha(n_0 - 1)(\nu + 1)l_2$$
$$+ [l_1 + C_\alpha(n_0 - 1)(\nu + 1)l_3]T \qquad (60)$$

i.e. equivalent to Equation 46, by defining

$$\chi_0 = l_0 + C_\alpha(n_0 - 1)(\nu + 1)l_2 \qquad (61)$$

and

$$\chi_1 = l_1 + C_\alpha(n_0 - 1)(\nu + 1)l_3 \qquad (62)$$

For the sake of simplicity C_α is set equal to 1 [17] and, since for YAG $\nu = 0.25$ and $n_0 \sim 1.8$, Equations (61) and (62) therefore become

$$\chi_0 = l_0 + l_2 \qquad (63)$$

and

$$\chi_1 = l_1 + l_3 \qquad (64)$$

l_0, l_1, l_2 and l_3 are obtained from a best fit of Equations (58) and (59) to measured data, as reported by Furuse et

al. [20] for a single-crystal YAG (except the dn/dT coefficient at RT, the data of which were for ceramic YAG). Their values are listed in Table 2.

Table 2 Fit parameters for the linear model of the thermo-optic coefficient.

Range	$l_0 \left[\frac{10^{-6}}{K}\right]$	$l_1 \left[\frac{10^{-8}}{K^2}\right]$	$l_2 \left[\frac{10^{-6}}{K}\right]$	$l_3 \left[\frac{10^{-8}}{K^2}\right]$
CT	-2.3[a]	3.8[a]	0.18[b]	2.1[b]
RT	3.4[c]	1.7[c]	4.2[d]	0.62[d]

References: a- [21], b- [6], c- [20] and d- [22].

Note the dn/dT data were obtained using a 633 nm He-Ne laser [20], however, for a real understanding of the lens power it would need to be evaluated with data measured at the laser wavelength. As reported by Sato and Taira [22] at RT, for example, at a wavelength of 1064 nm the dn/dT value is 12.1 10^{-6}/K, $\sim 50\%$ higher than the value at 633 nm.

The lens power in Figure 16 at a heatsink temperature $T_c > 125$ K in the CT range should be taken with caution, since in this case the maximum temperature of the rod no longer belongs to the CT range and the fit parameters T_0, k_0 and m_{CT} are not strictly valid anymore (see Figures 6 and 8).

6 Conclusion

In this paper we have drawn on the fact that the thermal conductivity of laser gain media are dependent upon
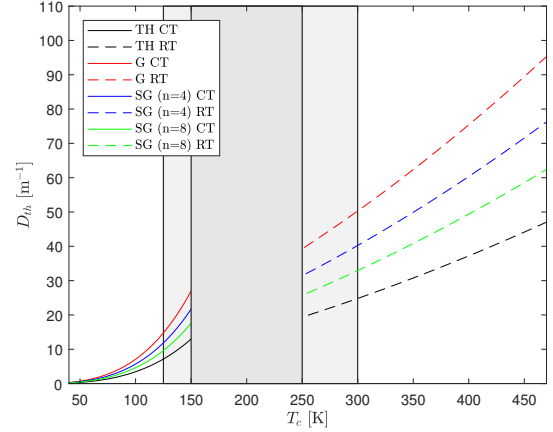
Fig. 16 Thermal lens dioptric power in CT and RT ranges for Top-hat, Gaussian and super-Gaussian pumping distributions.

their temperature. Consequently, solving the heat conductance equation, using the Kirchhoff integral transform, analytical expressions were derived for a number of realistic pumping sources, typically used in end-pumped rod-laser configurations. We compare the solutions obtained with exemplars from literature and show that in the limit of a constant thermal conductivity there is a natural convergence.

Through the power of having an analytical solution, we show that the temperature rise at the center of the laser rod has a dependence on the thermal impedance of the boundary layer, as is intuitively expected. In contrast with accepted expressions, these solutions predict an additional temperature rise associated with the thermal conductance parameter h. With this expression guidance on the minimum acceptable value for h for a set of design parameters can be obtained.

Lastly analytical expressions for the thermal lens diop-

tric power are derived in the limit of perfect boundary conditions. Intimately connected with the temperature dependence of the thermal conductivity, in the limit of a constant k_0, the expressions once again converge to their simplified analogues for Gaussian or top-hat pumping distributions.

It is evident that the solutions derived herein, for the typical parameters chosen, demonstrate a higher temperature rise than those obtained with temperature-independent thermal conductivity reported previously. Having analytical expressions that can be used for a range of temperatures provides a powerful set of tools for designing future end-pumped laser systems. This will be especially relevant to laser systems operating at cryogenic temperatures.

Appendices

Appendix A: Calculation of the temperature distribution in a top-hat end-pumped laser rod

In the case of top-hat pumping and considering the inner region of the laser rod, $0 \leq r \leq a$, Equation (6) becomes

$$\frac{1}{r}\frac{dU_1(r,z)}{dr} + \frac{d^2U_1(r,z)}{dr^2} = -Q_0 e^{-\alpha z} \qquad (65)$$

where the subscript 1 indicates that we are focusing just on the inner region.

Let $\dfrac{dU_1(r,z)}{dr} = \nu_1(r)$, which gives $\dfrac{d^2U_1(r,z)}{dr^2} = \dfrac{d\nu_1(r)}{dr}$.
Multiply both sides by r and substitute $1 = \dfrac{dr}{dr}$, giving

$$\frac{dr}{dr}\nu_1(r) + r\frac{d\nu_1(r)}{dr} = -Q_0 e^{-\alpha z} r \qquad (66)$$

So Equation (66) corresponds to

$$\frac{d}{dr}[r\nu_1(r)] = -Q_0 e^{-\alpha z} r \qquad (67)$$

and performing an integration in both sides one obtains

$$r\nu_1(r) = -\frac{Q_0 e^{-\alpha z}}{2}r^2 + A \qquad (68)$$

where A is a constant of integration, which must be found with a boundary condition. Dividing both sides by r, Equation (68) becomes

$$\nu_1(r) = \frac{dU_1(r,z)}{dr} = -\frac{Q_0 e^{-\alpha z}}{2}r + \frac{A}{r} \qquad (69)$$

and, with another integration, it returns

$$U_1(r,z) = -\frac{Q_0 e^{-\alpha z}}{4}r^2 + A\ln(r) + B \qquad (70)$$

where B is another constant of integration. By the definition of $U(r)$, Equation (7),[1]

$$\frac{k_0}{T_0^m(m+1)}T_1^{m+1}(r,z) = -\frac{Q_0 e^{-\alpha z}}{4}r^2 + A\ln(r) + B \tag{71}$$

which gives

$$T_1(r,z) = \left\{\left[-\frac{Q_0 e^{-\alpha z}}{4}r^2 + A\ln(r) + B\right]\frac{T_0^m(m+1)}{k_0}\right\}^{\frac{1}{m+1}} \tag{72}$$

For the outer region of the rod, $a < r \le b$, Equation (6) becomes

$$\frac{1}{r}\frac{dU_2(r,z)}{dr} + \frac{d^2 U_2(r,z)}{dr^2} = 0 \tag{73}$$

and it gives a solution of the form

$$U_2(r,z) = D\ln(r) + E \tag{74}$$

and then

$$T_2(r,z) = \left\{[D\ln(r) + E]\frac{T_0^m(m+1)}{k_0}\right\}^{\frac{1}{m+1}} \tag{75}$$

Now the boundary equations must be used to find the constants of integration A, B, D and E.

For reasons of symmetry, the amount of heat conducted per unit area (heat flux) in the r direction must be equal to 0 at the rod center, i.e.

$$-k(T)\left.\frac{dT_1}{dr}\right|_{r=0} = 0 \tag{76}$$

---

[1] For the sake of simplicity, we set the constant of integration C of Equation (7) equal to zero. It's easy to see, for example by Equation (81), that its value does not contribute to the calculation of the temperature distribution.

Substituting Equation (5) into Equation (76) and using the chain rule of differentiation, the first boundary condition (76) becomes:

$$-\left.\frac{dU_1}{dr}\right|_{r=0} = 0 \tag{77}$$

and, by Equation (69), it gives

$$A = 0 \tag{78}$$

At the external surface of the rod, $r = b$, the boundary condition is chosen instead to be [15]:

$$-\left.\frac{dU_2}{dr}\right|_{r=b} = h\left[T_2(r=b) - T_c\right] \tag{79}$$

Substituting in Equations (74) and (75), it returns

$$\frac{D}{bh} = T_c - \left\{[D\ln(b) + E]\frac{T_0^m(m+1)}{k_0}\right\}^{\frac{1}{m+1}} \tag{80}$$

Finally the continuity of the temperature and its derivative at $r = a$ is imposed, i.e.

$$T_1(r=a) = T_2(r=a) \tag{81}$$

which gives

$$-\frac{Q_0 e^{-\alpha z}}{4}a^2 + B = D\ln(a) + E \tag{82}$$

and

$$\left.\frac{dT_1}{dr}\right|_{r=a} = \left.\frac{dT_2}{dr}\right|_{r=a} \tag{83}$$

which gives

$$-\frac{Q_0 e^{-\alpha z}a}{2}\left[\frac{T_0^m(m+1)}{k_0}\left(-\frac{Q_0 e^{-\alpha z}a^2}{4} + B\right)\right]^{-\frac{m}{m+1}} =$$
$$\frac{D}{a}\left[\frac{T_0^m(m+1)}{k_0}(D\ln(a) + E)\right]^{-\frac{m}{m+1}} \tag{84}$$

Equations (80), (82) and (84) can be solved to find B, D and E and substituting their values in Equations (72) and (75), one obtains

$$T_1(r,z) = \left\{ F_0 e^{-\alpha z} \left[1 - \frac{r^2}{a^2} + \ln\left(\frac{b^2}{a^2}\right) \right] + \left(T_c + \frac{\eta_h P_{\text{in}} \alpha e^{-\alpha z}}{2\pi bh} \right)^{m+1} \right\}^{\frac{1}{m+1}} \quad (85)$$

$$T_2(r,z) = \left[F_0 e^{-\alpha z} \ln\left(\frac{b^2}{r^2}\right) + \left(T_c + \frac{\eta_h P_{\text{in}} \alpha e^{-\alpha z}}{2\pi bh} \right)^{m+1} \right]^{\frac{1}{m+1}} \quad (86)$$

Appendix B: Analytical calculation of the thermal lens dioptric power in the case of top-hat pumping

The integrals in Equation (50) can be analytically solved with two changes of variable. Here only the steps used to solve the first one are shown since the other integral can be solved in exactly the same way.

We therefore consider

$$I_1 = \frac{2\chi_0 F_0}{a^2(m+1)} \cdot \int_0^L e^{-\alpha z} \left\{ F_0 \left[1 + \ln\left(\frac{b^2}{a^2}\right) \right] e^{-\alpha z} + T_c^{m+1} \right\}^{-\frac{m}{m+1}} dz \quad (87)$$

Introducing $u = -\alpha z$ $(du = -\alpha dz)$

$$I_1 = -\frac{2\chi_0 F_0}{a^2 \alpha (m+1)} \cdot \int_0^L e^u \left(F_0 \left[1 + \ln\left(\frac{b^2}{a^2}\right) \right] e^u + T_c^{m+1} \right)^{-\frac{m}{m+1}} du \quad (88)$$

and using a new change of variable

$$w = F_0 \left[1 + \ln\left(\frac{b^2}{a^2}\right) \right] e^u + T_c^{m+1}$$

$\left(dw = F_0 \left[1 + \ln\left(\frac{b^2}{a^2}\right) \right] e^u du \right)$, one obtains

$$I_1 = -\frac{2\chi_0}{a^2(m+1)\alpha \left[1 + \ln\left(\frac{b^2}{a^2}\right) \right]} \cdot \int_0^L w^{-\frac{m}{m+1}} dw = -\frac{2\chi_0}{a^2 \alpha \left[1 + \ln\left(\frac{b^2}{a^2}\right) \right]} \left[w^{\frac{1}{m+1}} \right]_0^L \quad (89)$$

so

$$I_1 = \frac{2\chi_0}{a^2 \alpha \left[1 + \ln\left(\frac{b^2}{a^2}\right) \right]} \cdot \left[\left(F_0 e^{-\alpha z} \left[1 + \ln\left(\frac{b^2}{a^2}\right) \right] + T_c^{m+1} \right)^{\frac{1}{m+1}} \right]_L^0 \quad (90)$$

References

1. A. Giesen and J. Speiser, IEEE Journal of Selected Topics in Quantum Electronics **13,** (2007) 598-609.

2. D. J. Richardson, J. Nilsson, W. A. Clarkson, Journal of the Optical Society of America B - Optical Physics **27,** (2010) B63-B92.

3. T. S. Rutherford, W. M. Tulloch, E. K. Gustafson and R. L. Byer, IEEE Journal of Quantum Electronics **36,** (2000) 205-219.

4. W. A. Clarkson, Journal of Physics D: Applied Physics **34,** (2001) 2381-2395.

5. S. Chénais, F. Duron, S. Forget, F. Balembois and P. Georges, Progress in Quantum Electronics **30,** (2006) 89-153.

6. R. L. Aggarwal, D. J. Ripin, J. R. Ochoa and T. Y. Fan, Journal of Applied Physics **98,** (2005) 103514-1-103514-14.

7. M. H. Moghtader Dindarlu, A. Maleki, H. Saghafifar, M. Kavosh Tehrani and S. Baghali, Laser Physics **25,** (2015) 045001-045009.

8. K. R. Bagnall, Y. S. Muzychka and E. N. Wang, IEEE Transaction on Components, Packaging and Manufacturing Technology **4,** (2014) 408-420.

9. N. Hodgson and H. Weber, IEEE Journal of Quantum Electronics **29,** (1993) 2497-2507.

10. L. Cini, W. O. S. Bailey, Y. Yang and J. I. Mackenzie, "Temperature-dependent Analytical Thermal Model for End-pumped Solid-state Lasers", JM5A.5 at Advanced Solid State Lasers (ASSL), OSA (2017) Nagoya, Japan.

11. Y. Sato, J. Akiyama and T. Taira, Optical Materials **31,** (2008) 720-724.

12. T. Y. Fan, D. J. Ripin, R. L. Aggarwal, J. R. Ochoa, B. Chann, M. Tilleman and J. Spitzberg, IEEE Journal of Selected Topics in Quantum Electronics **13,** (2007) 448-459.

13. S. J. Yoon and J. I. Mackenzie, Optics Express 22, (2014) 8069-8075.

14. M. E. Innocenzi, H.T. Yura, C.L. Fincher and R.A. Fields, Applied Physics Letters **56,** (1990) 1831-1833.

15. A. Cousins, IEEE Journal of Quantum Electronics **28,** (1992) 1057-1069.

16. J. W. Kim, J. I. Mackenzie, J. R. Hayes, and W. A. Clarkson, Optics Express **19,** (2011) 14526-1453.

17. S. Bjurshagen and R. Koch, Applied Optics **43,** (2004) 4753-4767

18. D. J. Kim, S. H. Noh, S. M. Ahn and J. W. Kim, Optics Express **25,** (2017) 14668-14675.

19. N. Hodgson and H. Weber, "Laser Resonators and Beam Propagation", 2nd Edition, Chapter 13.2.6, pp. 476-487, Springer-Verlag, 2005.

20. H. Furuse, R. Yasuhara, and K. Hiraga, Optical Materials Express **4,** (2014) 1794-1799.

21. R. Wynne, J. L. Daneu, and T. Y. Fan, Applied Optics **38,** (1999) 32823284.

22. Y. Sato and T. Taira, Optical Materials Express **4,** (2014) 876-888.